

Locomotion of tensegrity robot through bar-length modulation: simulation and dynamic analysis

Received 3 September 2025, Revised 20 October 2025, Accepted 10 November 2025, Published online 22 November 2025

Keywords: six-bar tensegrity robots, bar driven, multi-body analysis software

Tensegrity robots represent a groundbreaking advancement in robotic design, offering advantages such as lightweight construction, self-deformation, and fold-ability. Thanks to their interesting properties, this type of structure can be used, for example, in space applications. This study focuses on the modelling and simulation of a six-bar tensegrity robot. A mathematical framework is developed using node-generalized coordinates and connection matrices, and a design scheme is proposed where movement is driven by altering bar lengths. The robot's movement was simulated using the multibody dynamics simulation software MSC ADAMS. The robot achieves locomotion through self-rolling, driven by controlled changes in bar lengths that shift the centre of gravity, demonstrating reduced energy consumption and improved structural stability compared to string-driven models. The design ensures stability and control by maintaining horizontal contact of actuated bars with the ground, preserving geometric configurations like squares or diamonds. In the article, in addition to the results of simulation tests, a robot control algorithm based on the tensegrity structure was proposed.

1. Introduction

The topic of robots using the concept of tensegrity structure is the subject of research work by many scientific centres. They pioneered the exploration of dynamic tensegrity structures, conducting detailed studies through physical hardware experiments and computational simulations. The scientific efforts have focused on detailed analyses conducted via these two complementary approaches, advancing the understanding and application of tensegrity robotics [1]. In other works, we can find methods of describing and constructing free-standing structures using axially

¹Wroclaw University of Science and Technology, Wroclaw, Poland



[☑] Jarosław SZREK, email: jaroslaw.szrek@pwr.edu.pl

loaded compression elements arranged within a carefully constructed network of tension elements. This type of arrangement is known as a tensegrity structure (short for tensile integrity). In such structures, each component is subjected exclusively to either pure axial compression or pure tension [2]. Tensegrity robot is a type of mobile robot that uses the concept of tensegrity, a structural principle that involves a network of compressive and tensile elements to create a lightweight yet flexible and stable structure. The robot consists of rigid bars (often called struts) and a series of connecting cables under tension. This setup enables the robot to absorb and distribute forces efficiently, making it ideal for applications where robustness and adaptability to uneven terrain are required. The tensegrity structures are independent of gravity, meaning they do not need to be anchored or supported by any surface to maintain stability [3]. These characteristics make them well-suited for aerospace and robotic applications.

From a robotics standpoint, another key advantage of tensegrity structures is the diffusion of forces. Unlike traditional serial manipulators, they lack lever arms, preventing torque accumulation at joints. Instead, forces are distributed across multiple load paths, enhancing the structure's robustness and resilience to mechanical failures. The springs in the robot structure should be mentioned. Thanks to them, the structure becomes more resistant to the effects of force impulses, e.g., during a fall. Research has explored vibration-driven locomotion using single-actuated tensegrity structures [4]. The study utilized finite element analysis (FEA) via ANSYS software to simulate dynamic behaviours of two prototypes; a planar and a spatial tensegrity configuration. The dynamic responses to varying driving frequencies and prestress levels were assessed, identifying their influence on locomotion performance. Experimental validation was conducted with physical prototypes to confirm the simulation findings, focusing on achieving bidirectional locomotion with minimal control complexity. Related work has been carried out on utilizing vibration-based actuation for small tensegrity systems [5]. To support this design, mathematical models were created to describe the interactions among nodes, bars, and strings. Simulations using a multi-body analysis environment MSC ADAMS software provided valuable insights into motion paths, dynamic stability, and overall system efficiency, showcasing the benefits of bar-driven mechanisms compared to string-based systems, but they only used single bar actuation mechanisms.

Another innovative advanced example of tensegrity robot was SUPPERball introduced by NASA, featuring six bars and twenty-four strings, where the strings functioned as the robot's actuators [6]. As a result, the robot's movement is energy intensive, inefficient, and difficult to control. Similarly a Real2Sim2Real (R2S2R) strategy has been introduced for Control of Cable Driven tensegrity robotics [7]. Similar structure was introduced by using bars as driving components rather than strings, addressing issues related to energy efficiency and structural resilience found in earlier models [8]. In addition, a bar-driven locomotion mechanism that enhances stability and reduces energy consumption is proposed [9]. Their research demonstrated that controlling the length of two base bars in contact with the ground

can effectively drive the robot. In parallel, energy-based optimization has been employed which improve trajectory planning with minimal control complexity [10].

A novel four-bar tensegrity robot was designed to simplify structural complexity while maintaining efficient locomotion [11]. The structure was modelled mathematically using node generalized coordinates and connection matrices, capturing the relationships among rigid bars, elastic cables and diagonal actuation elements. Simulations in multi-body analysis environment MSC ADAMS software provided insights into the rolling dynamics, showing that a complete rolling cycle involved eight discrete steps. However, deviations in the trajectory were observed, resulting from elastic collisions and spring-induced jitter during ground contact, highlighting challenges in achieving dynamic stability and precise control.

Path planning algorithms, such as A*, have also been utilized to optimize navigation, ensuring efficient movement in rolling tensegrity robots [12]. Recently, the integration of Pneumatic Artificial Muscles (PAMs) has enabled efficient planar motion, enhancing the stability of quadrupedal robots in various environments [13]. In addition, the Port-Hamiltonian framework offers a more accurate model by considering internal forces and environmental interactions, improving control in real-world applications [14]. Another example of recently advanced tensegrity robotics is the rimless-wheel-like tensegrity walker (RTW), which combines the stability of rimless wheels with the flexibility of tensegrity for efficient movement across varied terrains [15]. Likewise, TICBot utilizes tensegrity structures to navigate confined spaces, offering superior manoeuvrability compared to traditional robots [16]. Furthermore, hybrid model-based and deep reinforcement learning approaches improve control efficiency, enabling effective rolling on varied surface [17]. The application of tensegrity structures in robotics is well-established, with recent studies concentrating on their statics [18, 19], kinematics [20, 21], dynamic simulations [22–24], and workspace exploration [25–27]. These control strategies, actuation, and modelling advancements continue to drive tensegrity robotics toward more efficient, adaptable, and practical real-world applications.

This study introduces a six-bar tensegrity robot that achieves locomotion through bar-length modulation, unlike most prior works that rely on string or cable actuation. In addition, the paper presents a comprehensive mathematical framework using node and connection matrices, a realistic multi-body simulation in MSC ADAMS, and a step-function-based control strategy and bar actuation method that enables continuous rolling through a twelve-step actuation sequence. Finally, the inclusion of dynamic analysis of joint displacement, velocity, and contact forces goes beyond many earlier studies, making this work a distinctive contribution to tensegrity robotics.

2. Mathematical model

The six-bar tensegrity structure shown in Fig. 1 is made up of 12 nodes, 6 bars, and 24 cables (in our case, the six-bar components of the simulation model

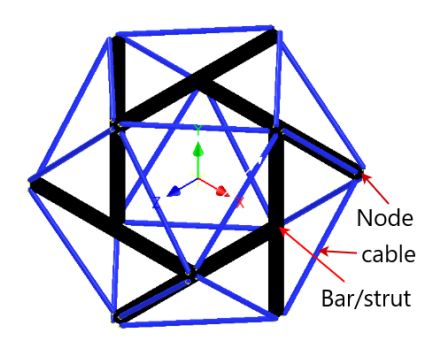


Fig. 1. Six bar tensegrity robot structural model. Nodes (the connecting point of black bar and blue thin members), bars/struts (black thick members), and cables (blue thin members; modelled as springs in the simulation)

were substituted with six translation pairs, and we also used springs instead of string), which are divided into three distinct groups to create a well-organized framework. In each group, the bars lie within a single plane and the three planes are oriented perpendicular to one another, ensuring a balanced and symmetrical arrangement. As shown in Fig. 2, these three orthogonal planes correspond to the coordinate planes of a Cartesian coordinate system. The intersection of these planes defines the origin of the coordinate system. This arrangement highlights the precise geometric design of tensegrity structure, where the bars and cables work together within this spatial configuration to maintain stability, symmetry, and structural efficiency.

In this configuration, the strings experience only tensile forces, while the bars are subjected to compressive stresses. These opposing forces work in harmony to ensure the structural stability of the system. This balance between tension and compression allows the tensegrity structure to maintain its form and effectively resist external loads. Furthermore, the bars in this tensegrity model are all of equal length, contributing to the symmetry and uniformity of the structure. Each bar is connected at its ends to nodes, which are evenly distributed across the surface of the structure. This arrangement ensures that the forces are evenly distributed, further enhancing the stability and resilience of the structure under various conditions.

Mathematical modelling of a tensegrity structure begins with the definition of its nodes, which serve as connection points for the bars and strings. The spatial coordinates of these nodes determine the position of each structural element. By classifying nodes according to specific rules, a node matrix can be constructed to represent each node category. These individual matrices are then combined into a complete tensegrity node matrix. As shown in Fig. 2, the structure consists of three mutually perpendicular planes, each containing one group of bars and four nodes. The distance between parallel bars is represented by d, while the length of each bar is denoted as ls.

Locomotion of tensegrity robot through bar-length modulation: simulation and . . .

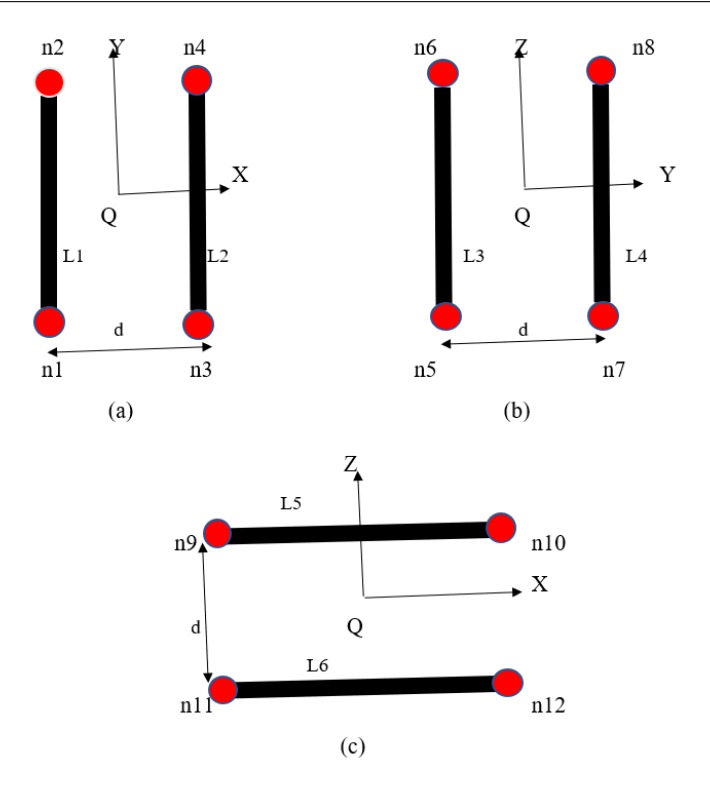


Fig. 2. Layout of the six-bar grouped into three orthogonal planes in Cartesian coordinate system: (a) YQX plane between bar L_1 and L_2 , (b) ZQY plane between bar L_3 and L_4 , (c) ZQX plane between bar L_5 and L_6

2.1. Node matrix

The coordinate vector for each node in the XQY plane is specified as follows. These coordinates define the precise positions of the nodes in relation to the XQY plane

$$n_{1} = \begin{bmatrix} n_{1x} & n_{1y} & n_{1z} \end{bmatrix}^{T} = \begin{bmatrix} -0.5d & -0.5ls & 0 \end{bmatrix}^{T},$$

$$n_{2} = \begin{bmatrix} n_{2x} & n_{2y} & n_{2z} \end{bmatrix}^{T} = \begin{bmatrix} -0.5d & 0.5ls & 0 \end{bmatrix}^{T},$$

$$n_{3} = \begin{bmatrix} n_{3x} & n_{3y} & n_{3z} \end{bmatrix}^{T} = \begin{bmatrix} 0.5d & -0.5ls & 0 \end{bmatrix}^{T},$$

$$n_{4} = \begin{bmatrix} n_{4x} & n_{4y} & n_{4z} \end{bmatrix}^{T} = \begin{bmatrix} 0.5d & 0.5ls & 0 \end{bmatrix}^{T},$$
(1)

where $n_i = [n_{ix}, n_{iy}, n_{iz}]^T$ is the 3-D coordinate vector of node i; d is the spacing between the two bars in the plane (mm); ls is the length of the bar (mm); $(\cdot)^{T}$ denotes transpose.



From equation (1), the positions of all nodes within the XQY plane can be systematically represented using a node matrix

$$N_1 = \begin{bmatrix} n_1 & n_2 & n_3 & n_4 \end{bmatrix}_{3 \times 4}, \tag{2}$$

where $N_1 \in \mathbb{R}^{3\times 4}$ is the node matrix for the XQY plane; n_j are the node position vectors defined in equation (1); $[\cdot]_{3\times 4}$ indicates the matrix dimensions.

Similarly, the coordinate vector for each node located within the ZQY plane is

$$n_{5} = \begin{bmatrix} n_{5x} & n_{5y} & n_{5z} \end{bmatrix}^{T} = \begin{bmatrix} 0 & -0.5d & -0.5ls \end{bmatrix}^{T},$$

$$n_{6} = \begin{bmatrix} n_{6x} & n_{6y} & n_{6z} \end{bmatrix}^{T} = \begin{bmatrix} 0 & -0.5d & 0.5ls \end{bmatrix}^{T},$$

$$n_{7} = \begin{bmatrix} n_{7x} & n_{7y} & n_{7z} \end{bmatrix}^{T} = \begin{bmatrix} 0 & 0.5d & -0.5ls \end{bmatrix}^{T},$$

$$n_{8} = \begin{bmatrix} n_{8x} & n_{8y} & n_{8z} \end{bmatrix}^{T} = \begin{bmatrix} 0 & 0.5d & 0.5ls \end{bmatrix}^{T}.$$
(3)

The positions of all nodes within the ZQY plane can be represented by:

$$N_2 = \begin{bmatrix} n_5 & n_6 & n_7 & n_8 \end{bmatrix}_{3 \times 4}, \tag{4}$$

where $N_2 \in \mathbb{R}^{3\times 4}$ is the node matrix for the ZQY plane; n_j are the node position vectors defined in equation (3).

The coordinate vector for each node located within the ZQX plane is defined as:

$$n_{9} = \begin{bmatrix} n_{9x} & n_{9y} & n_{9z} \end{bmatrix}^{T} = \begin{bmatrix} -0.5ls & 0 & 0.5d \end{bmatrix}^{T},$$

$$n_{10} = \begin{bmatrix} n_{10x} & n_{10y} & n_{10z} \end{bmatrix}^{T} = \begin{bmatrix} 0.5ls & 0 & 0.5d \end{bmatrix}^{T},$$

$$n_{11} = \begin{bmatrix} n_{11x} & n_{11y} & n_{11z} \end{bmatrix}^{T} = \begin{bmatrix} -0.5ls & 0 & -0.5d \end{bmatrix}^{T},$$

$$n_{12} = \begin{bmatrix} n_{12x} & n_{12y} & n_{12z} \end{bmatrix}^{T} = \begin{bmatrix} 0.5ls & 0 & -0.5d \end{bmatrix}^{T}.$$
(5)

The node matrix consisting of the positions of all nodes within the ZQX plane can be represented by

$$N_3 = \begin{bmatrix} n_9 & n_{10} & n_{11} & n_{12} \end{bmatrix}_{3 \times 4}, \tag{6}$$

where $N_3 \in \mathbb{R}^{3 \times 4}$ is the node matrix for the ZQX plane; n_j are the node position vectors defined in equation (5).

The node matrix for the entire tensegrity structure, which incorporates the positions of all nodes in the system, is given as:

$$N = \begin{bmatrix} N_1 & N_2 & N_3 \end{bmatrix}_{3 \times 12},\tag{7}$$

where $N \in \mathbb{R}^{3 \times 12}$ stacks all node coordinates by column-wise concatenation of N_1 , N_2 , and N_3 ; N_1 , N_2 , N_3 are the node matrices for the XQY, ZQY, and ZQX planes, respectively.

Therefore, the matrix representing the complete set of node positions is fully defined as:

$$N = \begin{bmatrix} n_{1x} & n_{2x} & n_{3x} & n_{4x} & n_{5x} & n_{6x} & n_{7x} & n_{8x} & n_{9x} & n_{10x} & n_{11x} & n_{12x} \\ n_{1y} & n_{2y} & n_{3y} & n_{4y} & n_{5y} & n_{6y} & n_{7y} & n_{8y} & n_{9y} & n_{10y} & n_{11y} & n_{12y} \\ n_{1z} & n_{2z} & n_{3z} & n_{4z} & n_{5z} & n_{6z} & n_{7z} & n_{8z} & n_{9z} & n_{10z} & n_{11z} & n_{12z} \end{bmatrix}, (8)$$

where n_{ix} , n_{iy} , n_{iz} are the x-, y-, and z-coordinates (of units mm) of node n_i for i = 1, ..., 12; rows correspond to axes x, y, and z, and columns correspond to nodes n_1-n_{12} .

2.2. Component matrix

The spatial positions of the nodes determine the component vectors of the structure. Therefore, using the information provided in the node matrix, the coordinates of the bars can be accurately calculated. From the picture shown in Fig. 2, the coordinates of the nodes associated with each bar can be determined. Let L_i denote the vector representing each bar, wich can be derived using the positions of its corresponding nodes

$$L_i = n_{2i} - n_{2i-1}, \text{ where } i \in \{1, 6\},$$
 (9)

where L_i is the vector of bar i (from node n_{2i-1} to node n_{2i}), $i \in \{1, ..., 6\}$; n_j are node position vectors as defined above. Therefore, in the XQY plane we have

$$L_1 = n_2 - n_1$$
 and $L_2 = n_4 - n_3$, (10)

where L_1 and L_2 are the bar vectors in the XQY plane, connecting node pairs (n_1, n_2) and (n_3, n_4) , respectively.

The rod matrix corresponding to the plane can be expressed as

$$R_1 = \begin{bmatrix} L_1 & L_2 \end{bmatrix}_{3 \times 2},\tag{11}$$

where $R_1 \in \mathbb{R}^{3 \times 2}$ is the rod matrix for the XQY plane, whose columns are the bar vectors L_1 and L_2 ; $L_i \in \mathbb{R}^3$ is the vector of bar i (compression member).

Thus, R_1 organizes the vector components of the two bars in the XQY plane into a single matrix for compact representation. So, the matrix R_1 can be represented by

$$R_1 = \begin{bmatrix} n_2 - n_1 & n_4 - n_3 \end{bmatrix}_{3 \times 2}.$$
 (12)

This can be rewritten in the following matrix form

$$R_{1} = \begin{bmatrix} n_{1} & n_{2} & n_{3} & n_{4} \end{bmatrix} \begin{bmatrix} -1 & 0 \\ 1 & 0 \\ 0 & -1 \\ 0 & 1 \end{bmatrix}.$$
 (13)

From the equation (13), R_1 can be expressed in terms of the node matrix N_1 and a connection matrix [28], which defines the relationships between the nodes and bars $C_{R_1}^T$:

$$R_1 = N_1 C_{R1}^T. (14)$$

Similarly, the rod matrix corresponding to the ZQY plane can be expressed as:

$$R_2 = \begin{bmatrix} L_3 & L_4 \end{bmatrix}_{3 \times 2},\tag{15}$$

where $R_2 \in \mathbb{R}^{3 \times 2}$ is the rod matrix for the ZQY plane, whose columns are the bar vectors L_2 and L_3 . Therefore, by utilizing the node matrix N_2 and a connection matrix C_{R2}^T the expression can be written as:

$$R_2 = N_2 C_{R2}^T. (16)$$

In a similar manner, the rod matrix associated with the ZQX plane can be defined as in equation (17).

$$R_3 = \begin{bmatrix} L_5 & L_6 \end{bmatrix}_{3 \times 2}. \tag{17}$$

The bar matrix in the XOZ plane can also be represented as the product of the node matrix and a constant matrix, as

$$R_3 = N_3 C_{R3}^T. (18)$$

Therefore, the rod matrix of the whole complete tensegrity structure can be represented by:

$$R = \begin{bmatrix} R_1 & R_2 & R_3 \end{bmatrix}_{3 \times 6},\tag{19}$$

where $R \in \mathbb{R}^{3\times 6}$ is the rod matrix of the complete structure; $R_1, R_2, R_3 \in \mathbb{R}^{3\times 2}$ are the rod matrices of the three orthogonal planes, each containing the two bar vectors

of that plane. Therefore, the rod matrix for the entire structure can be represented as the product of the node matrix and the connection matrix:

$$R = NC_R^{\mathrm{T}},\tag{20}$$

where $N = [N_1 \ N_2 \ N_3] \in \mathbb{R}^{3 \times 12}$ stacks all node coordinates (see equation (7); $C_R \in \mathbb{R}^{12 \times 6}$ is the overall connection (incidence) matrix that encodes the bar–node relationships; thus $C_R^\mathsf{T} \in \mathbb{R}^{12 \times 6}$ and $R = N \ C_R^\mathsf{T} \in \mathbb{R}^{3 \times 6}$.

$$C_R^{\mathsf{T}} = \begin{bmatrix} C_{R1}^T & 0 & 0\\ 0 & C_{R2}^T & 0\\ 0 & 0 & C_{R3}^T \end{bmatrix}_{12 \times 6} . \tag{21}$$

The string matrix is derived following a similar approach, utilizing the connection matrix as its basis. The relationship between the nodes and the strings is comprehensively presented in Table 1, clearly depicting their interconnections and structural dependencies.

			•		_			
String	S_1	S_2	S_3	S_4	S_5	S_6	S_7	S_8
Starting point	n_5	n_5	n_5	n_6	n_6	n_7	n_3	n_9
End point	n_4	n_2	n_{11}	n_{10}	n_9	n_{12}	n_{10}	n_8
String	S ₉	S_{10}	S_{11}	S_{12}	S_{13}	S_{14}	S_{15}	S_{16}
Starting point	n_1	n_1	n_7	n_8	n_3	n_9	n_2	n_5
End point	n_{11}	n_7	n_3	n_1	n_8	n_2	n_{11}	n_2
String	S ₁₇	S_{18}	S_{19}	S_{20}	S_{21}	S_{22}	S_{23}	S_{24}
Starting point	n9	n_{10}	n_6	n_{12}	n_5	n_{12}	n_7	n_{10}
End point	n_1	n_8	n_4	n_4	n_{12}	n_3	n_{11}	n_4

Table 1. Relationships between strings and nodes

Table 1 defines the relationship between the node matrix and the string matrix through their interconnected properties, highlighting the structural dependencies within the tensegrity system. This relationship forms the foundation for mathematical modelling, enabling precise representation of the structure's configuration and dynamics. It can be expressed as follows:

$$S = NC_S^{\mathrm{T}},\tag{22}$$

where $S \in \mathbb{R}^{3 \times 24}$ is the string (cable) matrix whose k-th column is the oriented vector of string S_k ; $N \in \mathbb{R}^{3 \times 12}$ is the node matrix stacking the coordinates of nodes n_1, \ldots, n_{12} (see equation (7)); $C_S \in \mathbb{R}^{12 \times 24}$ is the string connection (incidence) matrix with entries $(C_S)_{k,i} = +1$ at the starting node of string S_k , $(C_S)_{k,j} = -1$ at its end node, and 0 otherwise (node pairs as listed in Table 1); $C_S^T \in \mathbb{R}^{12 \times 24}$ is its transpose.

3. Simulation of the tensegrity robot

The simulation model of the six-bar tensegrity robot developed using the multibody analysis environment MSC ADAMS software is illustrated in Fig. 3. The geometric node coordinates and material parameters for the robot's components are detailed in Table 2 and Table 3, providing comprehensive insights into the structural configuration and material properties.

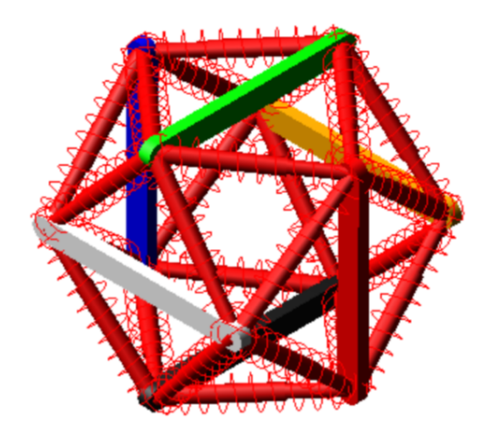


Fig. 3. Six bar tensegrity robot simulation model in multi-body analysis environment

To ensure the simulation's accuracy, the model is designed such that the weight, centre of gravity, movement inertia, and product of inertia for each component are equivalent to those of the corresponding components in the physical structure. The simulation results closely align with the robot's real-world behaviour by maintaining this equivalence. This congruence ensures that the dynamic response, stability, and overall performance observed in the simulation accurately represent the actual characteristics of the robot, making it a reliable tool for analysing and optimizing the design and functionality of the tensegrity structure.

Loc-y Loc-y **Nodes** Loc-x Loc-z **Nodes** Loc-x Loc-z -90 0 -1000 100 -90 n_7 n_1 0 -10090 0 100 90 n_2 n_8 100 -900 -90100 n_3 n_9 100 90 0 90 0 100 n_4 n_{10} 0 -90-900 -100-100 n_5 n_{11} 0 0 -10090 90 -100 n_6 n_{12}

Table 2. Simulation model geometric node coordinates

Table 3. Material parameters of the robot's components

Parameter	Value				
Bar length	180 mm				
The distance between parallel bar	200 mm				
Bar weight	150 g				
Spring stiffness coefficient	5 N/mm				
Damping coefficient	$8 \times 10^{-2} \mathrm{N \cdot s/mm}$				
Spring preload	10 N				
Static friction coefficient	0.9				
Dynamic friction coefficient	0.7				

The precise positioning of each node is determined by specifying the coordinates of the node. The connections between nodes are established using these coordinates, thereby defining the arrangement of bars and strings within the structure. The simulation model also incorporates elastic springs as the string components, requiring the specification of relevant parameters for these elements. The stiffness and damping coefficients of the springs play a critical role in determining the robot's ability to maintain self-equilibrium in the absence of external forces. Additionally, including a spring preload provides initial prestress to the robot's components. By adjusting the preload value, the equilibrium stability of the tensegrity robot can be fine-tuned, ensuring the desired structural balance and performance. To provide a clear understanding of the simulation model, Table 2 outlines the detailed node coordinates used in its configuration, while Table 3 provides the material parameters of the robot's components, ensuring clarity in the structural and material properties of the model.

The robot must roll continuously for twelve rotations to complete one full cycle. For clarity within the multi-body analysis environment, the six pairs of bar groups are labelled as shown in Fig. 3. During every 5 seconds, the maximum extension occurs on the same end face, with one pair of bars extending to a maximum length of 260 mm, while the other pair remains at its original length of 180 mm.

3.1. Design scheme and control strategy

Building upon the previous analysis, the six-bar tensegrity structure is developed. Any change in the structure's shape results in a shift in its overall centre of gravity; if the centre of gravity moves away from the ground, the structure initiates a rolling motion, enabling locomotion [29]. Following this principle, the six-bar tensegrity structure is oriented on its side and adapted into a six-bar tensegrity robot capable of achieving movement through self-rolling.

The rolling motion of the six-bar tensegrity robot is achieved by altering the lengths of the bars, which drives changes in the structure's overall shape. As the six-bar tensegrity structure deforms, the lengths of the connected springs also vary accordingly. The bars are designed to expand and contract as required to ensure that the robot's shape transformation remains controllable.

This design enables the robot to alter its entire structural configuration by actuating the bars located at its end faces. To maintain precise control over the robot's shape, the bar which is always in horizontal contact with the ground undergoing actuation. Additionally, to change the direction of movement, the bar positioned opposite to the intended direction is actuated. This approach ensures that the robot consistently retains a defined geometric configuration, such as a square or diamond, thereby preserving stability and controllability during motion. To alter the structural configuration, we use a step function (Fig. 4) STEP(x, x_0 , h_0 , x_1 , h_1) that interpolates between two markers using a cubic polynomial [30]. The equation governing the STEP function is given below.

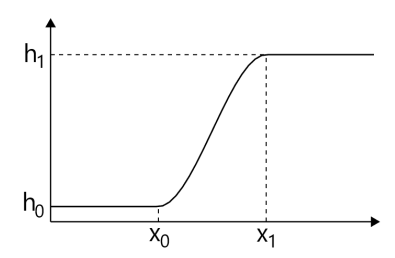


Fig. 4. Step function graph

STEP =
$$\begin{cases} h_0, & \text{when } x \le x_0, \\ h_0 + (h_1 - h_0) \left[\frac{x - x_0}{x_1 - x_0} \right]^2 \left\{ 3 - 2 \frac{x - x_0}{x_1 - x_0} \right\}, & \text{when } x_0 \le x \le x_1, \\ h_1, & \text{when } x \ge x_1. \end{cases}$$
(24)

Figs. 5 and 6 present the centre of mass and translational displacement of Link 1 in a six-bar tensegrity structure, with the motion governed by the step function equation (24), which smoothly varies the length of the bar. Fig. 5 shows



the centre of mass trajectory for Link 1 along Y-axis from (0 to 10 sec). The graphs indicate a smooth and symmetric displacement profile, suggesting a controlled and continuous motion. Similarly Fig. 6 show the translational displacement of Link 1 extending up to 80 mm and then returning to its original position. This suggests that the extension and contraction of the bars directly influence the displacement characteristics of the mechanism.

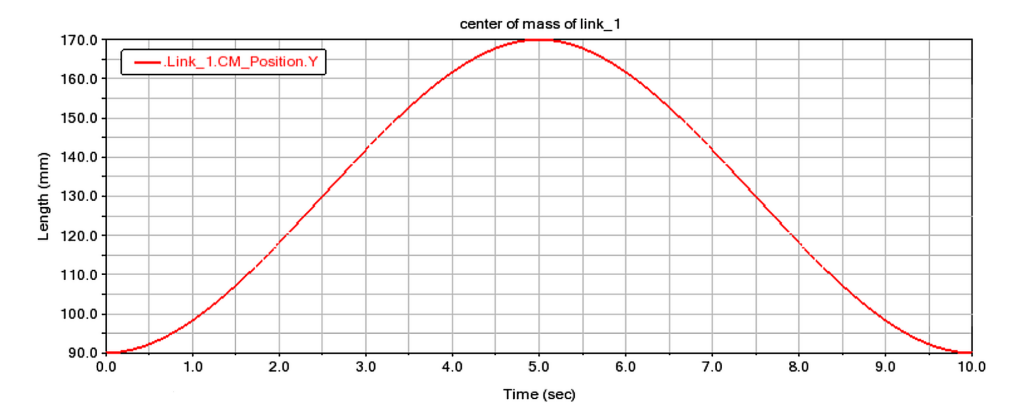


Fig. 5. Centre of mass of Link 1 along Y-axis

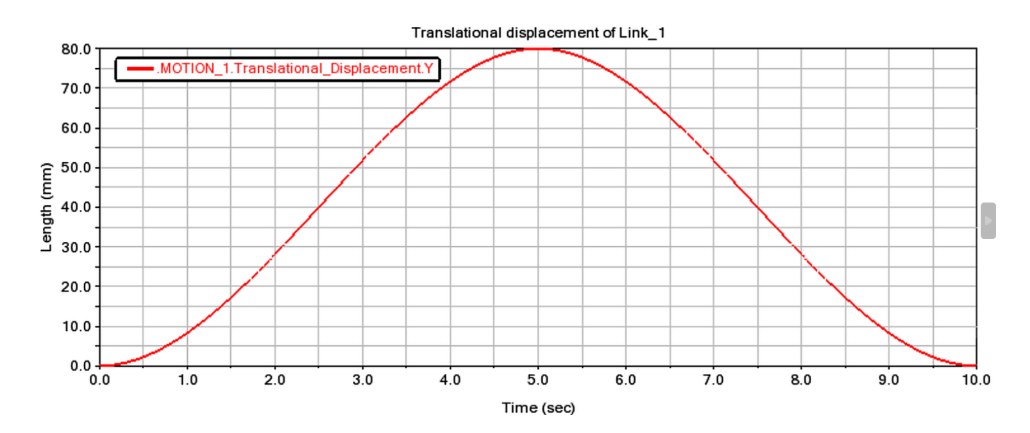


Fig. 6. Translational displacement of Link 1 along Y-axis

Based on this mechanism, we implemented a sequence of twelve steps, effectively completing six full rotations of the six-bar tensegrity robot. The controlled variation in bar length, governed by the step function shown in Fig. 7, facilitates smooth rolling motion, enabling efficient locomotion over multiple cycles.

The motion cycle of the six-bar tensegrity robot spans 60 seconds, and the robot's rolling motion can be divided into twelve steps with each step of movement lasting 5 seconds, as shown in Table 4. The symbol '+' indicates that the extendable bar is stretched, while the symbol '-' signifies that the bar is contracted. The symbol

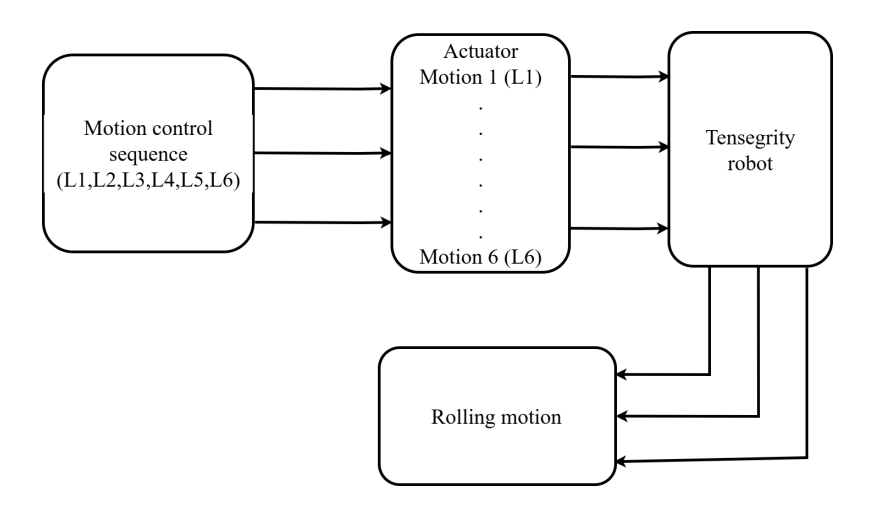


Fig. 7. Schematics of control strategy

'0' indicates that the length of the extendable bar remains constant. These twelve steps effectively complete six full rotations of the robot. Upon completing the six rotations, the robot returns to its original configuration shown in Fig. 10 (see Section 3.3).

Time	0–30 s						30-60 s					
Time	0–5	5-10	10-15	15-20	20-25	25-30	30–35	35-40	40–45	45-50	50-55	55-60
L_1	+	-	0	0	0	0	0	0	+	-	0	0
L_2	0	0	+	_	0	0	0	0	0	0	0	0
L_3	0	0	0	0	+	-	0	0	+	_	0	0
L_4	0	0	0	0	0	0	+	_	0	0	+	-
L_5	0	0	0	0	0	0	0	0	0	0	+	-
L_6	+	_	0	0	0	0	0	0	0	0	0	0

Table 4. The actuation sequence for the extendable bar along X-axis

3.2. Quantitative locomotion and efficiency metrics

Geometry and rolling radius. From the node layout (Table 2) and component parameters (Table 3), the half-spans are $d/2 = 100 \,\mathrm{mm}$ and $l_s/2 = 90 \,\mathrm{mm}$. A contact node lies at

$$R = \sqrt{(d/2)^2 + (l_s/2)^2} = \sqrt{100^2 + 90^2} = 134.53 \text{ mm.}$$
 (25)

Hence, the circumference is

$$C = 2\pi R = 0.8453 \text{ m},$$
 (26)

where R is rolling radius; d is the spacing between the two bars in the plane (mm); *ls* is the bar length (mm); C is circumference.



Distance per cycle and mean forward speed. With 6 rotations in 60 s (12 steps $\times 5 \text{ s}$), the forward distance is

$$D = 6C = 5.0718 \text{ m}, \qquad \bar{v} = \frac{D}{60} = 0.0845 \text{ m/s}.$$
 (27)

Rotation rate.

rps =
$$\frac{6}{60}$$
 = 0.10 rev/s, $\omega = 2\pi \text{ rps} = 0.6283 \text{ rad/s}.$ (28)

Normalized speeds. Defining body length as 2R, BL/s (the body-lengths per second) are

BL/s =
$$\frac{\bar{v}}{2R} = \frac{6 \cdot 2\pi R/60}{2R} = \frac{\pi}{10} = 0.3141 \text{ BL/s}.$$
 (29)

In bar-lengths per second:

$$\frac{\bar{v}}{l_s} = \frac{0.0845}{0.180} = 0.4696 \text{ bar-lengths/s.}$$
 (30)

Actuation stroke. Each event changes bar length by $\Delta L = 260 - 180 = 80$ mm over 5 s, i.e., 16 mm/s stroke rate. Table 4 contains $N_{\text{events}} = 18 \text{ "+/-"}$ marks in the 60 s cycle, so

$$\sum |\Delta L| = 18 \times 0.08 = 1.44 \text{ m}.$$
 (31)

Stroke-per-distance (SPD).

$$SPD = \frac{\sum |\Delta L|}{D} = \frac{1.44}{5.0718} = 0.2839,$$
 (32)

$$\frac{1}{\text{SPD}} = 3.5221 \text{ m forward per 1 m stroke.}$$
 (33)

The lower the SPD the more distance per actuation cycle. We include stroke-perdistance (SPD) = 0.284 m stroke per m forward as a size-independent efficiency proxy to enable cross-platform comparisons going forward.

3.3. Simulation result

This section reports the motion and force responses of the six-bar tensegrity robot over a 60 s cycle under the actuation schedule in Table 4. The results are organized from kinematics to contact/element forces and configuration evolution. The motion responses confirm that the bar–length actuation strategy yields smooth and periodic rolling. In Fig. 8a, the displacement curves indicate a periodic rolling motion, with peaks and valleys corresponding to the extension and contraction

of specific bars. The smooth progression of displacement suggests that the rolling motion is continuous and stable over the 60-second cycle. Similarly, Fig. 8b provides insights into the movement of individual joints over time. Each coloured curve corresponds to a specific joint's displacement. The repetitive pattern observed in the graph aligns with the cyclic actuation strategy, confirming that each joint undergoes a consistent and predictable movement pattern.

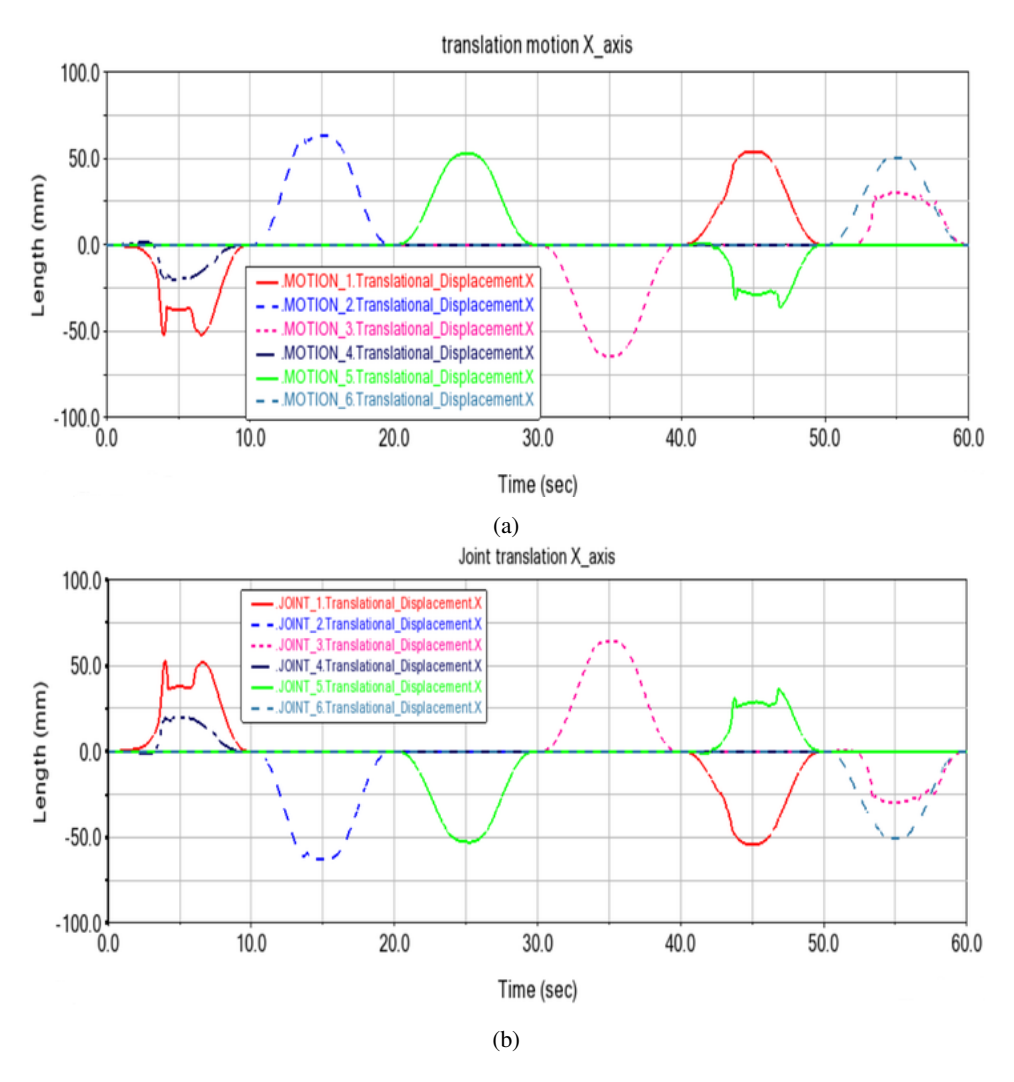


Fig. 8. Visualization of motion and joint translational displacement along the X-axis; (a) motion translational displacement, (b) joint translational displacement

One key observation from Fig. 8 is the inverse relationship between the motion translational displacement and the joint translational displacement resulting from the phase shift induced by the robot's rolling motion. The robot moves forward

through the alternating extension and contraction of its bars. As a particular bar extends, it pushes against the ground, causing the robot's body to roll forward, while the contraction of another bar shifts the centre of mass, altering the displacement of individual joints. This rolling motion introduces a rotational component, causing the individual joints to experience displacement in the opposite direction relative to the ground. This behaviour is similar to a rolling wheel where the top moves in the direction of travel while the bottom moves momentarily in the opposite direction relative to the ground. The actuation follows a sinusoidal, wave-like pattern, with joint displacement fluctuating over time. Consequently, when a joint reaches its maximum displacement (peak), the robot body is typically in a lower displacement phase and vice versa.

Fig. 9 presents the translational velocity magnitude of the link (L_1) at different time intervals. The peaks in Fig. 9a, indicate instances of rapid acceleration, corresponding to moments where (L_1) is actively extending and the initial ground interaction. The graph shows a sharp increase in velocity, suggesting that rapid accelerations or oscillations in Link 1's motion, likely due to transient forces or structural adjustments within the tensegrity system. The presence of multiple peaks indicates that Link 1 undergoes brief periods of high velocity, followed by deceleration and reorientation. In contrast, Fig. 9b highlights a moment where the velocity approaches zero, signifying a temporary pause in movement before transitioning into the next phase. These decay is due to internal tensions and damping redistribute loads, bringing the mechanism to a quasi steady regime between actuation steps. Therefore, reduction in velocity suggests that the system is approaching a more stable configuration after the initial oscillations. The damping effect observed here aligns with the expected behaviour of tensegrity structures, where oscillations eventually settle as internal forces and tensions balance out. These results confirm that the simulation captures the dynamic and stabilizing nature of the robot, with Link 1 transitioning from highly dynamic motion to a stable state over time. This behaviour is crucial for understanding and optimizing the control and stability of tensegrity robots during operation. This observation is consistent with the periodic

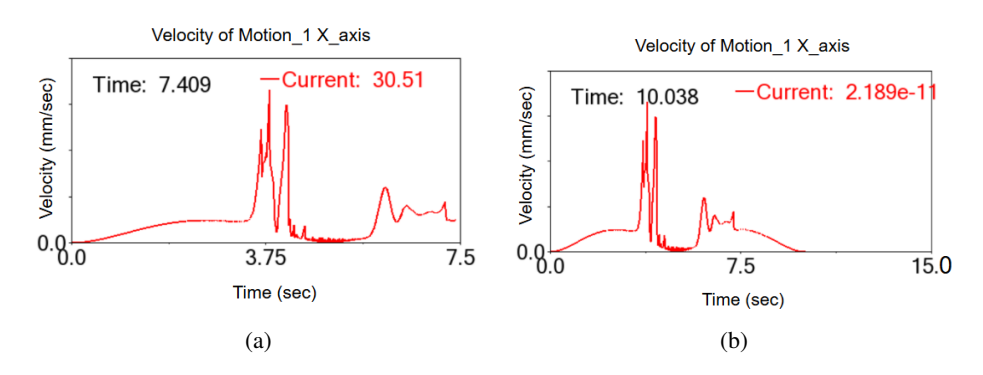


Fig. 9. Visualization of motion translational velocity of link one (L_1) along X-axis



motion cycle, as each bar undergoes alternating active (stretching/contracting) and passive (constant length) phases.

The drive mechanism forms the core of the robot's functionality, with bar-based actuation employed to control the tensegrity robot. By altering the lengths of all six bars, the robot can perform rolling motions and execute its intended movement tasks effectively. Fig. 10 presents the simulated motion visualization of the six-bar

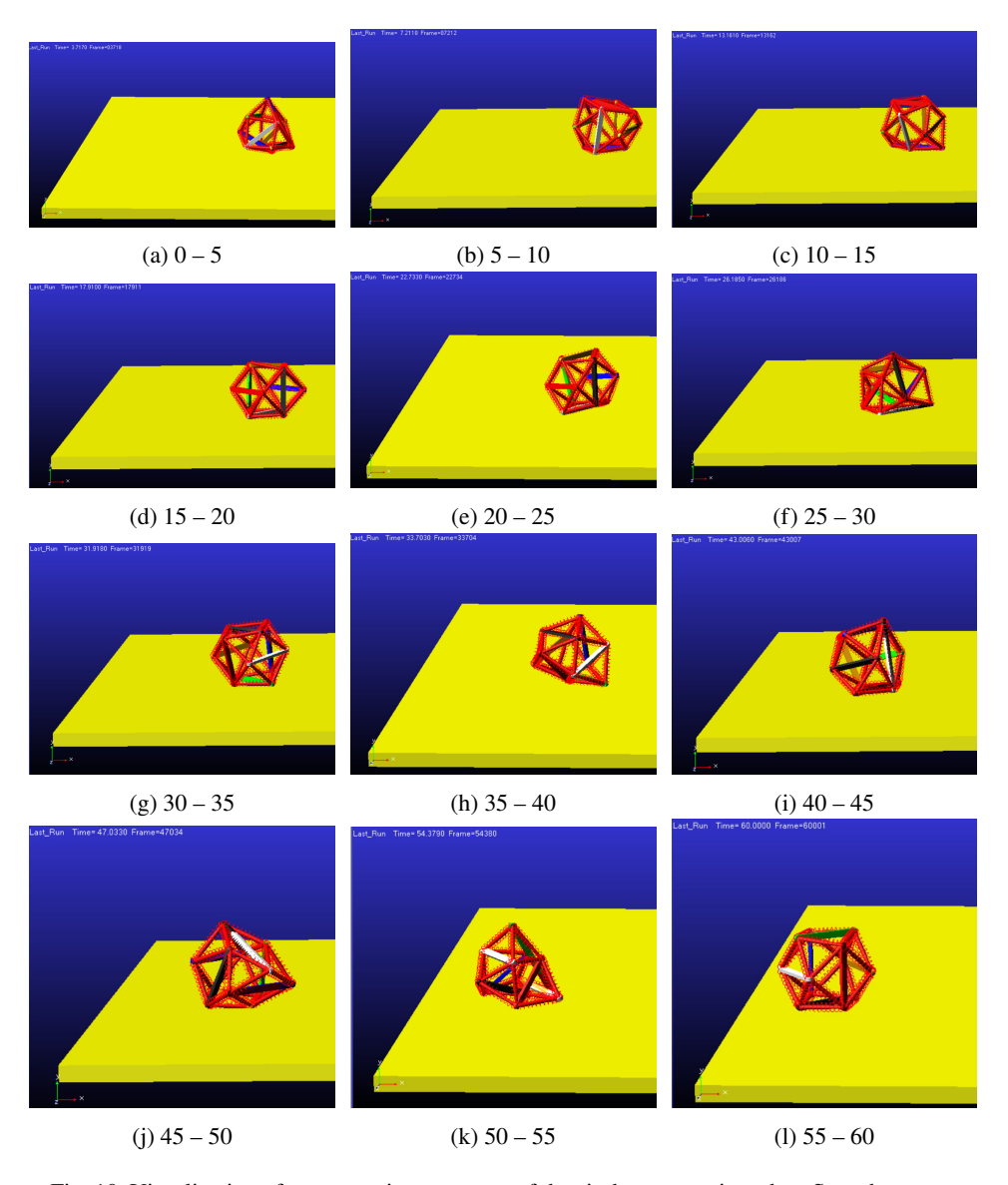


Fig. 10. Visualization of one actuation sequence of the six-bar tensegrity robot. Snapshots over consecutive 5 s windows illustrate the shape changes that produce locomotion

tensegrity robot based on the implemented driving scheme, demonstrating that the robot achieves overall movement through continuous rolling according to the control strategy.

Fig. 11 illustrates the displacement curve of the centre of gravity of the six bars along the X-axis direction. The trends observed in the graph show that the centre of gravity of the six bars undergoes noticeable displacement along the X-axis over time. As time advances, the displacement along the X-axis steadily increases, signifying the forward progression of the robot. This continuous increase in displacement confirms that, under the actuation provided by the bar, the six-bar tensegrity robot can achieve forward locomotion. Quantitatively, this trend corresponds to a mean normalized speed of 0.314 BL/s, placing our platform above the typical 0.010-0.250 BL/s reported for rolling spherical tensegrities [31] (e.g., ReCTeR at 0.250 BL/s) and indicating comparatively brisk translation for a bar-driven sixstrut design. At the same time, the required actuation remains conservative; a stroke rate of 16 mm/s, is in line with ~ 10 mm/s values commonly assumed in modelling studies and well below actuator capabilities reported for NASA SUPERball $(\leq 60 \text{ cm/s})$ [6]. Taken together, the steadily increasing X-axis displacement and the favourable speed-actuation profile confirm that the proposed bar-drive scheme enables controlled forward locomotion without aggressive actuation, supporting the robot's suitability for executing designed motion tasks efficiently.

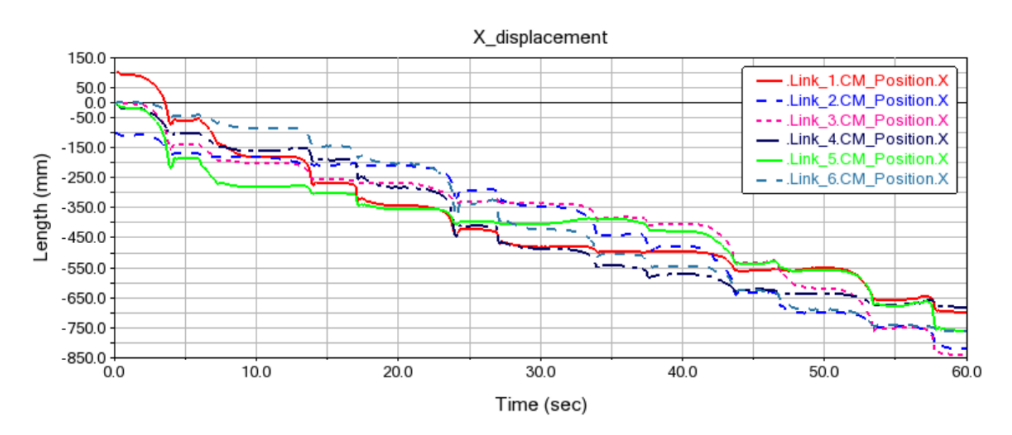


Fig. 11. The trajectory of the centre of gravity of the six bars along the X-axis

Fig. 12 shows the trajectory of the robot's centre of mass, displaying the magnitude of its motion path, along with the rotation axis position that allows the bars to adjust the direction of movement. This diagram provides insights into how the bars' adjustments influence the overall movement dynamics, highlighting the key role of rotational positioning in directing the robot's motion. The representation emphasizes the relationship between the centre of mass displacement and the bar rotations, demonstrating the robot's ability to manoeuvre effectively by altering its movement direction through strategic bar positioning. Additionally, the figure high-

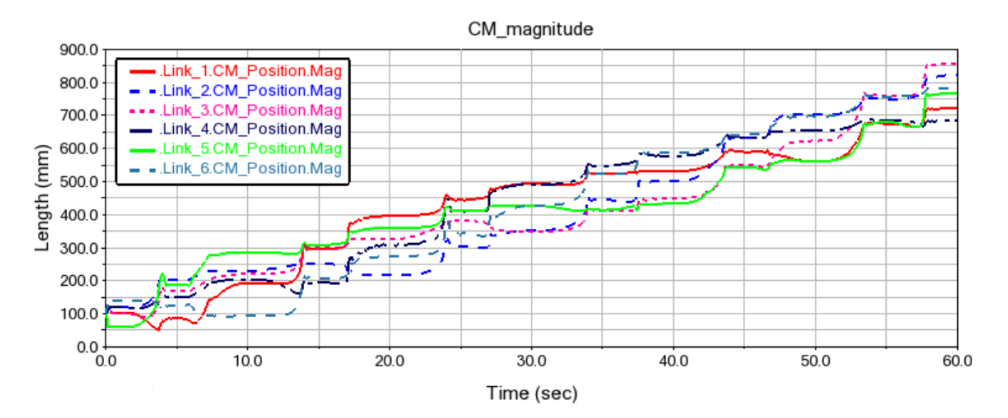


Fig. 12. The trajectory of the robot's centre of mass magnitude

lights that the robot's movement trajectory deviates from a straight path, revealing noticeable motion discrepancies.

Contact force variation of Link 1 is illustrated in Fig. 13 which is vertically aligned and forms a point contact with the ground in the six-bar tensegrity robot. The contact force magnitude experiences a sharp spike, suggesting that Link 1 momentarily undergoes a high-impact contact with the ground due to a sudden shift in load distribution. Similarly, in Fig. 14 the motion-induced element force also exhibits a peak at the same time, indicating a corresponding internal force reaction within the structure. This implies a marking phase where the link absorbs and transmits maximum force to sustain movement.

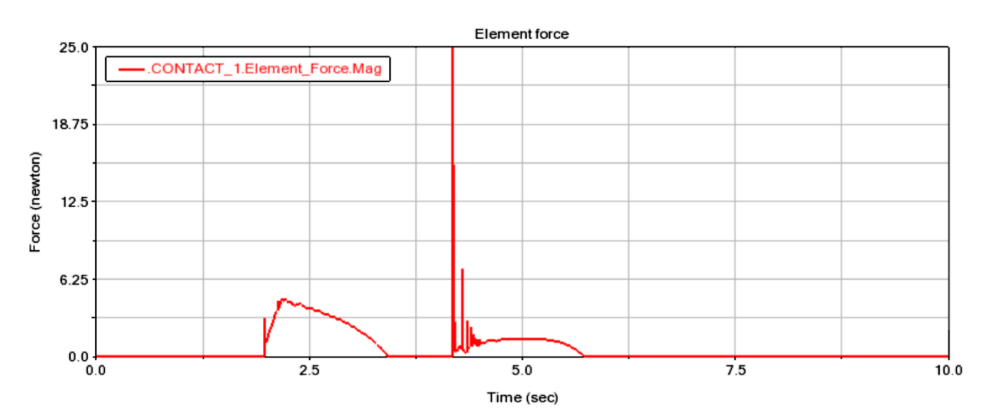
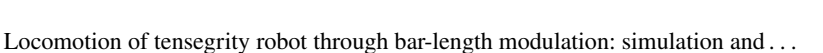


Fig. 13. Contact force variation of Link 1

Similarly, contact force variation of Link 6 is shown in Fig. 15. The results show that Link 6 which is horizontally aligned to the ground experiences a high contact force peak at the initial seconds due to a sudden impact when it first makes ground contact. This implies a rapid force application upon contact, which gradually stabilizes as the movement continues. In Fig. 16, the motion-induced element force



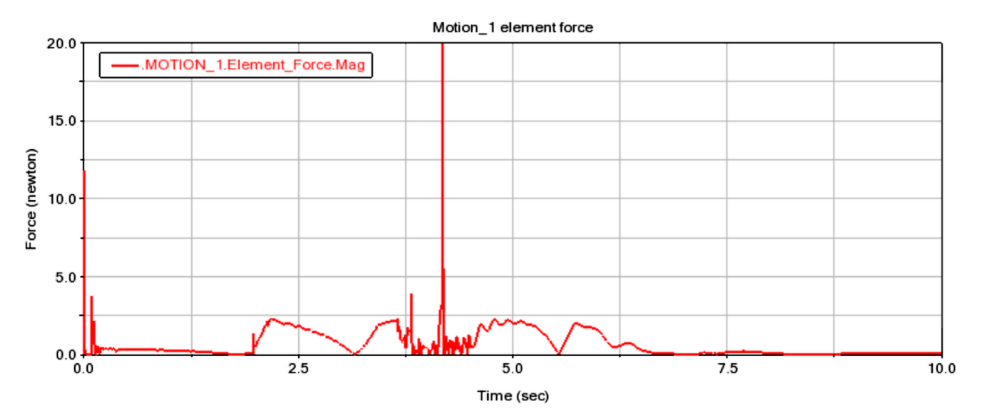


Fig. 14. Motion elemental force magnitude of Link 1

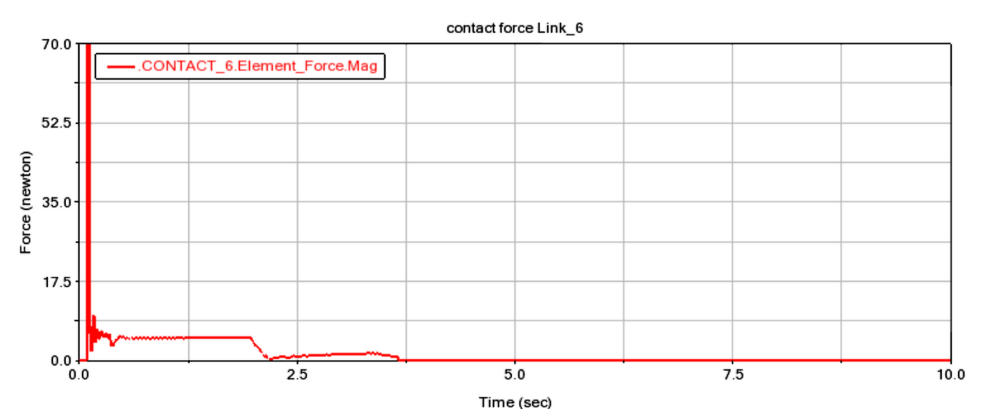


Fig. 15. Contact force variation of Link 6

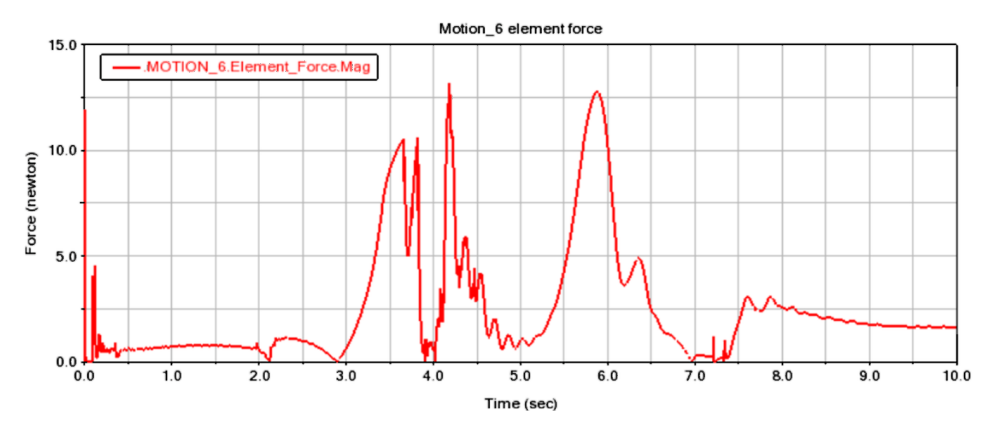


Fig. 16. Motion elemental force magnitude of Link 6

exhibits multiple oscillations, suggesting continuous force redistribution during rolling motion. These fluctuations result from structural deformations and shifting loads as the robot progresses. The observed force variations confirm that Link 6

plays a crucial role in absorbing and transmitting forces to maintain the rolling movement of the tensegrity robot. When selecting drives for the robot, especially its dynamic parameters, the interaction with the ground must be taken into account. Thanks to stimulation we can obtain, for example, guidelines for optimizing drive parameters. In particular, the contact force or the force course in the actuator well illustrate the required values.

4. Conclusion

This research successfully establishes the feasibility of a six-bar tensegrity robot for locomotion through bar-length modulation. The robot achieves stable, efficient, and continuous movement by implementing controlled adjustments to bar lengths while preserving its structural integrity. The simulation results validate the proposed design, confirming that bar-driven actuation enables precise motion control, enhanced mobility, and consistent performance across different conditions. Furthermore, observations of dynamic parameters, such as joint translation, motion, and contact force interaction with the ground, are critical in determining the appropriate drives for the robot.

Relative to prior rolling spherical tensegrities, our normalized speed sits above the commonly reported 0.010–0.250 BL/s range for string–driven platforms, yet is achieved without aggressive actuation, lower energy consumption, improved structural stability, and simplified control, highlighting the promise of bar–driven control for precise motion and robust ground interaction. These characteristics make tensegrity robots highly promising for applications requiring lightweight, resilient, and efficient mobility, such as planetary exploration, search and rescue.

Moreover, the study highlights the potential for further innovations in tensegrity robotics, including advanced control strategies, vibration reduction, real-world deployment, and material optimization to enhance performance. By applying the unique properties of tensegrity structures, future research can unlock new possibilities in autonomous locomotion, bio-inspired robotics, and adaptive robotic systems. This work contributes to the growing field of soft, reconfigurable and flexible robotics, demonstrating that tensegrity-based mechanisms can play a crucial role in the next generation of robotic solutions for space applications.

One of the directions of further work is to create a lab-scale prototype equipped with embedded sensors to benchmark energy use. The resulting data support system identification to refine contact and friction models, reducing impact-induced oscillations and lateral drift. Building on these models, energy-aware trajectory planning and drive optimization are developed. And also, passive and active damping are investigated to mitigate vibration. Together, these efforts culminate in a co-optimization of geometry, actuation, and control to validate simulation assumptions and to quantify real-world efficiency and robustness.



References

- [1] C. Paul, F.J. Valero-Cuevas, and H. Lipson. Design and control of tensegrity robots for locomotion. *IEEE Transactions on Robotics*, 22(5):944–957, 2006. doi: 10.1109/TRO.2006.878980.
- [2] R.B. Fuller. Synergetics: Explorations in the Geometry of Thinking. Macmillan Publishing Co., Inc., New York, 1982.
- [3] B. Nurimbetov, M. Issa, and H.A. Varol. Robotic assembly planning of tensegrity structures. In 2019 IEEE/SICE International Symposium on System Integration (SII), pages 73–78, 2019. doi: 10.1109/SII.2019.8700342.
- [4] V. Böhm and K. Zimmermann. Vibration-driven mobile robots based on single actuated tensegrity structures. In 2013 IEEE International Conference on Robotics and Automation (ICRA), pages 5475–5480, 2013. doi: 10.1109/ICRA.2013.6631362.
- [5] M. Khazanov, J. Jocque, and J. Rieffel. Developing morphological computation in tensegrity robots for controllable actuation. In *Proceedings of the Companion Publication of the 2014 Annual Conference on Genetic and Evolutionary Computation (GECCO Companion)*, pages 1049–1052, 2014. doi: 10.1145/2598394.2605680.
- [6] A.P. Sabelhaus, J. Bruce, K. Caluwaerts, P. Manovi, R. Fallah Firoozi, S. Dobi, A.M. Agogino, and V. SunSpiral. System design and locomotion of SUPERball, an untethered tensegrity robot. In 2015 IEEE International Conference on Robotics and Automation (ICRA), pages 2867–2873, 2015. doi: 10.1109/ICRA.2015.7139590.
- [7] K. Wang, W.R. Johnson, S. Lu, X. Huang, J. Booth, R. Kramer-Bottiglio, M. Aanjaneya, and K. Bekris. Real2Sim2Real transfer for control of cable-driven robots via a differentiable physics engine. In 2023 IEEE/RSJ International Conference on Intelligent Robots and Systems (IROS), pages 2534–2541, 2023. doi: 10.1109/IROS55552.2023.10341811.
- [8] A. Luo, H. Xin, P. Cao, X. Hao, Y. Yu, P. Sun, and W. Tian. Motion simulation of six-bar tensegrity robot based on ADAMS. In 2016 IEEE International Conference on Mechatronics and Automation (ICMA), pages 264–269, 2016. doi: 10.1109/ICMA.2016.7558572.
- [9] A. Luo, S. Che, and H. Liu. The driving of the six-bar tensegrity robot. In 2017 IEEE International Conference on Robotics and Biomimetics (ROBIO), pages 640–645, 2017. doi: 10.1109/ROBIO.2017.8324489.
- [10] S. Savin, O. Balakhnov, and A. Klimchik. Energy-based local forward and inverse kinematics methods for tensegrity robots. In 2020 Fourth IEEE International Conference on Robotic Computing (IRC), pages 280–284, 2020. doi: 10.1109/IRC.2020.00051.
- [11] A. Luo, J. Wang, and H. Liu. Four-bar tensegrity robot based on adams simulation. In 2017 IEEE International Conference on Mechatronics and Automation (ICMA), pages 1463–1468, 2017. doi: 10.1109/ICMA.2017.8016032.
- [12] J. Chang, B. Li, W. Liu, and W. Du. The path planning method of tensegrity robot based on A* algorithm, 2018. doi: 10.1109/CYBER.2018.8688187.
- [13] J. Lee, A. Coutinho, N. Oh, J. H. Jang, Y. J. Park, H. Namgung, D. G. Oh, and H. Rodrigue. Vacuum-driven class-2 tensegrity-based mechanism for quadrupedal robot motion. *IEEE Robotics and Automation Letters*, 9(7):6520–6527, 2024. doi: 10.1109/LRA.2024.3407410.
- [14] S. Liu, Q. Yang, J. Lv, and H. Fang. Modeling of a six-bar tensegrity robot using the port-hamiltonian framework and experimental validation. *IEEE Robotics and Automation Letters*, 9(5):4439–4446, 2024. doi: 10.1109/LRA.2024.3381819.
- [15] Y. Zheng, F. Asano, and C. Yan. Passive dynamic walking of a novel tensegrity robot combines contradictory properties: Stability and flexibility. In 2023 8th IEEE International Conference on Advanced Robotics and Mechatronics (ICARM), pages 37–42, 2023. doi: 10.1109/I-CARM58088.2023.10218880.

- [16] Y. Liu, Q. Bi, X. Dai, R. Song, J. Zhao, and Y. Li. Ticbot: Development of a tensegrity-based in-pipe crawling robot. IEEE Transactions on Industrial Electronics, 70(8):8184–8193, 2022. doi: 10.1109/TIE.2022.3224131.
- [17] Y. Guo and H. Peng. Full-actuation rolling locomotion with tensegrity robot via deep reinforcement learning. In 2021 5th International Conference on Robotics and Automation Sciences (ICRAS), pages 51–55, 2021. doi: 10.1109/ICRAS52689.2021.9476651.
- [18] L. Ervin and V. Vikas. Geometric static modeling framework for piecewise-continuous curvedlink multi point-of-contact tensegrity robots. IEEE Robotics and Automation Letters, 2024. doi: 10.1109/LRA.2024.3486199.
- [19] A.P. Sabelhaus, A.H. Li, K.A. Sover, J.R. Madden, A.R. Barkan, A.K. Agogino, and A.M. Agogino. Inverse statics optimization for compound tensegrity robots. IEEE Robotics and Automation Letters, 5(3):3982–3989, 2020. doi: 10.1109/LRA.2020.2983699.
- [20] J.M. Mirats-Tur and J. Camps. A three-DoF actuated robot. IEEE Robotics and Automation Magazine, 18(3):96-103, 2011. doi: 10.1109/MRA.2011.940991.
- [21] S. Liu, Q. Li, P. Wang, and F. Guo. Kinematic and static analysis of a Mechanism and Machine Theory, 149:103788, 2020. novel tensegrity robot. 10.1016/j.mechmachtheory.2020.103788.
- [22] W. Du, S. Ma, B. Li, M. Wang, and S. Hirai. Dynamic simulation for 6-strut tensegrity robots. In 2014 IEEE International Conference on Information and Automation (ICIA), pages 870–875, 2014. doi: 10.1109/ICInfA.2014.6932774.
- [23] C. Lin, D. Li, and Y. Zhao. Tensegrity robot dynamic simulation and kinetic strategy programming. In 2016 IEEE Chinese Guidance, Navigation and Control Conference (CGNCC), pages 2394–2398, 2016. doi: 10.1109/CGNCC.2016.7829167.
- [24] A. Zhakatayev, B. Abdikadirova, S. Sarmonov, and H.A. Varol. Dynamics of tensegrity robots with negative stiffness elements. IEEE Access, 8:187114–187125, 2020. doi: 10.1109/AC-CESS.2020.3031279.
- [25] X. Yuan, M. Lin, Z. Du, M. Zheng, H. Lei, Q. Chen, and Z. Ji. The influence of geometric parameters on the workspace of the 4-SPS TBPM. In 2022 2nd International Conference on Algorithms, High Performance Computing and Artificial Intelligence (AHPCAI), pages 134-138, 2022. doi: 10.1109/AHPCAI57455.2022.10087835.
- [26] S. Savin, O. Balakhnov, and A. Klimchik. Workspace analysis of tensegrity structures with an iterative energy-based algorithm. In 2020 International Conference Nonlinearity, Information and Robotics (NIR), pages 1-4, 2020. doi: 10.1109/NIR50484.2020.9290196.
- [27] Q. Boehler, I. Charpentier, M.S. Vedrines, and P. Renaud. Definition and computation of tensegrity mechanism workspace. Journal of Mechanisms and Robotics, 7(4):044502, 2015. doi: 10.1115/1.4029809.
- [28] H. Liu, X. Yang, and A. Luo. Three-bar tensegrity structure analysis of the axial folded way. In 2017 IEEE International Conference on Mechatronics and Automation (ICMA), pages 1320–1324, 2017. doi: 10.1109/ICMA.2017.8016008.
- [29] M. Shibata, F. Saijyo, and S. Hirai. Crawling by body deformation of tensegrity structure robots. In 2009 IEEE International Conference on Robotics and Automation (ICRA), pages 4375–4380, 2009. doi: 10.1109/ROBOT.2009.5152752.
- [30] Recurdyn documentation. https://functionbay.com/documentation/onlinehelp/default.htm# !Documents/step.htm.
- [31] J. Mo, H. Fang, and Q. Yang. Design and locomotion characteristic analysis of two kinds of tensegrity hopping robots. iScience, 27(3), 2024. doi: 10.1016/j.isci.2024.109226.